# First *in-vivo* Experiments with a Large field-of-view Flat Panel Photon-Counting Detector

Moiz Ahmad, Rebecca Fahrig, Martin Spahn, Jang-Hwan Choi,
Niko Köster, Silke Reitz, Waldo Hinshaw, Leland Pung, Teri Moore, Andreas Maier, and Kerstin Müller

***Abstract*—In the recent years, dual-energy CT becomes of more and more interest in clinical practice. The ability to distinguish different materials and tissue provides additional information to the clinician to make treatment decisions. Material decomposition for example allows to separate iodinated contrast agent from soft tissue due to its stronger enhancement at low photon energies compared to other materials that do not show this behavior. In conventional CT imaging several techniques are investigated for dual-energy imaging, whereas dual-energy imaging has not found its way into interventional C-arm CT imaging, yet. In the angiographic suite, discrimination of iodine from soft tissue would for example allow the generation of digital subtraction images without any motion artifacts. In this work, the first images generated with a large field-of-view photon-counting detector integrated into a clinical C-arm system have been investigated. The acquired 2D and 3D images of an *in-vivo* pig study look promising and open up the way for dual-energy imaging in the angiographic suite.**

## I. Introduction

### A. Purpose of this Work

One major goal in medical CT research today investigates the decomposition of the scanned object into its different materials. Dual-energy imaging allows to exploit the different absorption behavior of distinct materials and tissue under varying X-ray photon energies. For example, the attenuation of iodine, which is broadly used as intravascular contrast agent, decreases less than the attenuation of soft tissue with increasing photon energy. Possible clinical applications that benefit from this are, e.g. improved detection of a hyperenhancing malignancies in abdominal imaging [1], detection of endoleaks after endovascular aneurysm repair [2], distinguishing tumor bleed from pure hemorrhage [3] or coronary atherosclerotic plaque characterization [4]. In order to acquire images with different photon energies, multiple techniques can be applied: (i) acquisition of two consecutive scans with two different tube voltages, (ii) acquisition of a single scan using one X-ray tube with fast voltage switching, (iii) using a dual-or multilayer detector, (iv) acquisition with two (or more) X-ray tubes simultaneously with different voltage settings, and (v) using a photon-counting energy-discriminating detector with two or more energy thresholds [5]. In conventional CT, most of the previously mentioned approaches are integrated into clinical CT scanners from different vendors. However, photon-counting detectors are still on-going research in dual-energy CT and not clinical applicable, yet [6], [7].

In this work, the first setup of a customized manufactured large filed-of-view photon-counting detector mounted on a research clinical angiographic C-arm CT system is presented. The setup allows to acquire 2D energy discriminating images during 2D static and 3D rotational scans.

### B. State of the Art

Photon-counting detectors (PCDs) divide the transmitted X-ray spectrum into a number of different energy bins. The number of bins is highly dependent on the design and application of the distinctive detector. This principle varies completely from the conventional energy integrating detector that does not allow for energy differentiation. PCDs can help to overcome certain limitations of the current available detector technology, e.g. tissue-specific images to distinguish blood from contrast agent and/or to improve the signal-to-noise ratio by exploiting energy dependent image properties. The two most used materials to convert the absorbed photon energy of the emitted X-ray spectrum into an electrical signal are cadmium telluride (CdTe) and cadmium zinc telluride. The magnitude of the electrical signal is proportional to the incident photon's energy. In order to build a clinical applicable PCD for X-ray and CT imaging, some hardware design challenges need to be addressed. One major challenge is the pulse pileup due to the high peak X-ray flux in CT imaging. This means that pulses generated by coincident photons might be piled up and observed as one. This leads to a wrong detected energy, and a loss in the number of overall counts. There are many more challenges and a more detailed description can be found in [5], [7].

## II. Methods and Materials

### A. Photon-Counting Detector

In this paper, we investigated a large field-of-view dual-energy photon-counting detector for its application in interventional radiology. The detector is a customized OEM product manufactured by XCounter ABB (Danderyd, Sweden), hereafter referred to as "XCD" (Fig. 1a). In this detector, 1 mm cadmium telluride (CdTe) is used as conversion material from the X-ray energy to an electrical signal. The detector covers an active area of $30{\times}5$ cm$^2$ made up of several individual modules, each having a size of $1.25{\times}2.5$ cm$^2$. Overall the 2D image matrix is $3072{\times}512$ pixel with an isotropic resolution of 100 $\mu$m. The exposure integration range is from 100 $\mu$s-5 s. The XCD features two energy bins per pixel with adjustable thresholds with each counter on the pixel has a counter depth of 12 bit. Therefore, synchronous acquisition of a total energy

M. Ahmad, W. Hinshaw, and K. Müller are with the Radiological Sciences Lab, Department of Radiology, Stanford University, Stanford, CA, USA. E-mail: moiz@stanford.edu. R. Fahrig and J.-H. Choi were with the Radiological Sciences Lab, Department of Radiology, Stanford University, Stanford, CA, USA. R. Fahrig is now with Siemens Healthcare GmbH, Forchheim, Germany. M. Spahn, N. Köster, S. Reitz are with Siemens Healthcare GmbH, Forchheim, Germany. L. Pung and T. Moore are with Siemens Medical Solutions Inc, Malvern, USA. A. Maier is with the Pattern Recognition Lab, Department of Computer Science, Friedrich-Alexander-Universität Erlangen-Nürnberg, Germany.

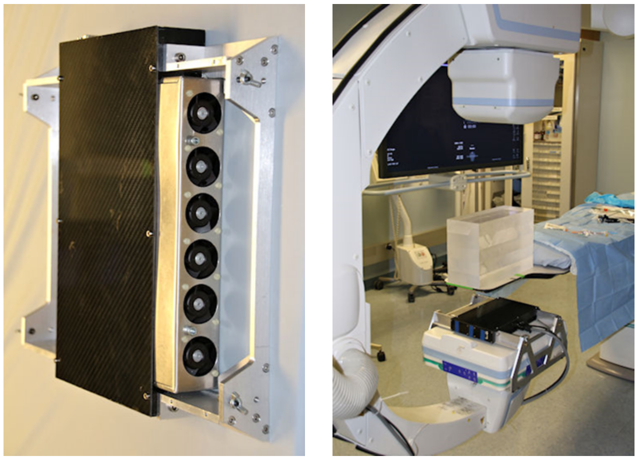

(a) (b)

Figure 1: (a) Large field-of-view photon-counting detector (XCD) and (b) mounted to an Artis zeego system (Siemens Healthcare GmbH, Forchheim, Germany).

(TE) and a high energy (HE) image can be performed. The detector also features a charge sharing correction feature to restore the energy that may spread over several neighboring pixel due to fluorescence or charge dispersion and to count the event only once. The detector design is similar to the small PCD presented in Ullberg et al. [8]. The readout is performed over a gigabit ethernet connection and the generated 2D images are visualized and stored on an external workstation.

In order to perform 2D and 3D clinical imaging, the XCD was "piggy-back" mounted to the flat panel detector (FD) of an Artis zeego system (Siemens Healthcare GmbH, Forchheim, Germany) (Fig. 1b). The clinical system's X-ray tube (MEGALIX CAT Plus) was used. A software application enables manual control of the tube current (mA), pulse width (ms), and voltage (kV).

### B. 2D Image Processing

The XCD provides the ability to acquire either 2D images from one static view or 2D images during a rotational scan. Both image stacks need to be processed to correct for gain variations, defect pixels, geometric deviations between individual detector modules, and count rate linearization. A rough overview of the image processing pipeline is given in Fig. 2. The first step is to correct for pixel wise variations in efficiency. For conventional FDs a flat-field correction can be applied, where multiplicative coefficients characterizing the relative efficiency of each pixel to the mean pixel efficiency can be found. However, the efficiency of each pixel is energy dependent, and this dependence is unique for each of them [9]. Hence, the detection efficiency depends individually on the local attenuation properties of the imaged sample, and consequently, a simple flat-field correction is not sufficient. Here, the signal-to-equivalent thickness calibration (STC) method presented by Vavrik et al. is applied to correct for variations in pixel efficiency [10]. The method also works for slightly different calibration and sample materials [9]. As a

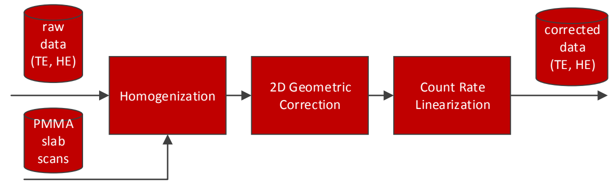


Figure 2: Overview of the image processing pipeline.

"calibrator" different thicknesses of polymethyl methacrylate (PMMA) slabs (1.18 g/cm$^2$) were used and imaged with specific exposure parameters equivalent to the later acquisitions. Additionally, a defect pixel correction step is applied. As a next step, minor gaps at the module edges are removed and the modules might be shifted in whole pixel steps to fit to the adjacent modules. Additionally, the butting zones around each module show high signal variations. These are homogenized by detection of the modules and whole butting pixel from neighboring pixels are introduced to approximate the gaps. Afterwards, a specifically designed count rate linearization algorithm is performed. Overall, this results in corrected TE and HE image stacks. The low energy (LE) image stack is generated by simple subtraction LE = TE-HE.

### C. 3D Image Reconstruction

The XCD mounted on the C-arm CT system provides the ability to acquire simultaneous photon-counting 2D images or image series from static projections or to reconstruct volumetric data from a cone-beam CT run. Since the mounting of the XCD onto the FD changes the pre-calibrated system trajectory, new 3D projection matrices need to be computed [11]. Due to the different extent of the XCD and the FD, a customized PDS-3 phantom was manufactured with slightly varying phantom diameter, height and adapted helical slope of the bead inserts (Fig. 3).

For 3D imaging a scan protocol with a duration of 10 s and 30 fps was used to acquire 248 (TE and HE) imaging stacks, distributed over 200° with an angular distance of 0.8°. The XCD projection images have a size of $3072\times512$ pixel with an isotropic pixel size of 100 $\mu$m. The source-to-detector distance measured 120 cm. For a preliminary image comparison, the same image protocol has been performed without the XCD mounted to the FD. The 2D FD projection images have a size of $1240\times960$ with an isotropic pixel size of 0.308 mm.

For 3D XCD image generation using the TE stack, the Feldkamp-Davis and Kress (FDK) algorithm with a shepp-logan ramp filter with a cut-off frequency of 0, quadratic cut-off strength, and a slope cut-off of 4.0, available in the CONRAD software package was used[12]. The FD images were sent to the external workstation from the clinical system and reconstructed with a matrix size of $512^3$ and a voxel size of 0.425 mm. One XCD reconstruction was performed using $1\times1$ native detector pixel size on a $512^2\times140$ matrix with an isotropic voxel size of 0.2125 mm. Another XCD reconstruction mimics the acquired FD data, with a $3\times3$ binning on the XCD and a reconstruction of a $512^2\times70$ volume with a voxel size of 0.425 mm.

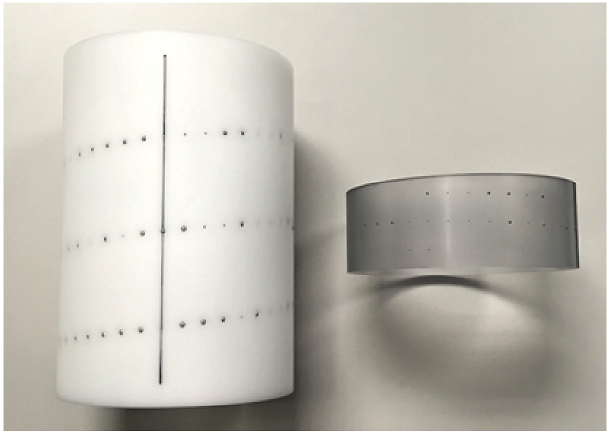

(a)

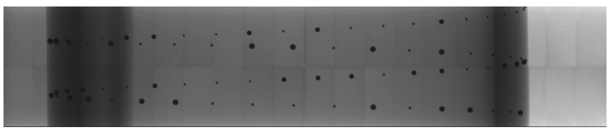

(b)

Figure 3: (a) PDS-2 and customized PDS-3 phantom. (b) TE image of PDS-3 phantom.

## III. Results

Stanford University's Administrative Panel on Laboratory Animal Care approved the protocol for this *in-vivo* animal study. One Yorkshire pig (approximately 50 kg) was used for this study. A self-expanding nickel–titanium, single-wire braid LVIS Jr stent (Microvention/Terumo, Tustin, California, US) was placed into the transverse facial artery. The LVIS Jr outer wire diameter is 0.0024" ($\approx$0.06 mm). The 3D acquisition was performed with requesting 81 kV, 12.5 ms and 150 mA from the X-ray tube and the thresholds of the XCD were set to 8 keV for the lower and 39 keV for the higher energy threshold. An example of one *in-vivo* corrected 2D image (TE, HE, and LE) from a rotational run is illustrated in Fig. 4. It can be seen that the image noise increases with a lower photon count rate. The butting zones are slightly visible in the HE and LE images. In Fig. 5 the 3D reconstructions of the *in-vivo* pig acquisitions are presented. The XCD data set shows the superior spatial resolution of the stent. But it also shows the impact of the visible butting zones transitions.

## IV. Conclusion

In this paper, the first setup of a large field-of-view photon-counting detector with an angiographic C-arm CT system has been presented. The acquired *in-vivo* pig images look promising and are a major step towards dual-energy imaging within the angiographic suite.

**Disclaimer:** The concepts and information presented in this paper are based on research and are not commercially available.

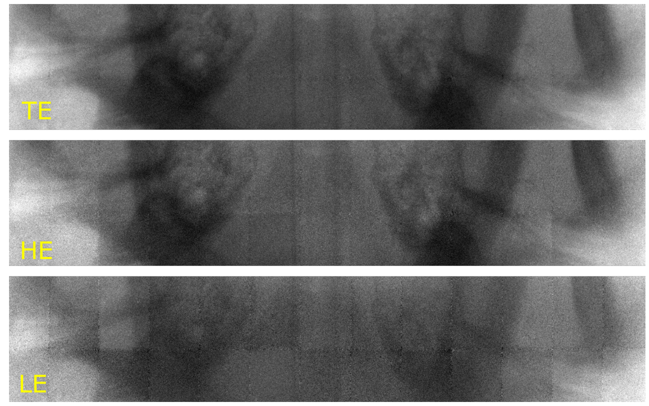


Figure 4: 2D anterior-posterior images of the *in-vivo* pig dataset from a 3D rotational scan after pre-processing.

## Acknowledgment

The authors gratefully acknowledge funding support from the NIH Shared Instrument Grant S10 RR026714 supporting the zeego@StanfordLab, and Siemens Healthcare GmbH Advanced Therapy. Special thanks also goes to Jeremy Heit, MD, PhD and Yamil Saenz for their help with the in-vivo pig experiment and to Microvention/Terumo, Tustin, California, US to provide the intracranial stent.

## References

[1] M. Anzidei, M. Di Martino, B. Sacconi, L. Saba, F. Boni, F. Zaccagna, D. Geiger, M. Kirchin, A. Napoli, M. Bezzi, and C. Catalano, "Evaluation of image quality, radiation dose and diagnostic performance of dual-energy CT datasets in patients with hepatocellular carcinoma," *Clinical Radiology*, vol. 70, no. 9, pp. 1–8, 2015.

[2] V. Buffa, A. Solazzo, V. D'Auria, A. Del Prete, A. Vallone, M. Luzietti, M. Madau, R. Grassi, and V. Miele, "Dual-source dual-energy CT: dose reduction after endovascular abdominal aortic aneurysm repair," *La radiologia medica*, vol. 119, no. 12, pp. 934–941, 2014.

[3] S. J. Kim, H. K. Lim, H. Y. Lee, C. G. Choi, D. H. Lee, D. C. Suh, S. M. Kim, J. K. Kim, and B. Krauss, "Dual-energy CT in the evaluation of intracerebral hemorrhage of unknown origin: Differentiation between tumor bleeding and pure hemorrhage," *American Journal of Neuroradiology*, vol. 33, no. 5, pp. 865–872, 2012.

[4] I. Danad, Z. A. Fayad, M. J. Willemink, and J. K. Min, "New Applications of Cardiac Computed Tomography," *JACC: Cardiovascular Imaging*, vol. 8, no. 6, pp. 710–723, 2015.

[5] C. H. McCollough, S. Leng, L. Yu, and J. G. Fletcher, "Dual- and Multi-Energy CT: Principles, Technical Approaches, and Clinical Applications.," *Radiology*, vol. 276, no. 3, pp. 637–653, 2015.

[6] Z. Yu, S. Leng, S. Jorgensen, Z. Li, R. Gutjahr, B. Chen, X. Duan, A. Halaweish, L. Yu, E. Ritman, and C. McCollough, "Initial results from a prototype whole-body photon-counting computed tomography system," in *Proceedings of SPIE Medical Imaging*, 2015.

[7] K. Taguchi and J. S. Iwanczyk, "Vision 20/20: Single photon counting x-ray detectors in medical imaging.," *Medical Physics*, vol. 40, no. 10, p. 100901, 2013.

[8] C. Ullberg, M. Urech, N. Weber, A. Engman, A. Redz, and F. Henckel, "Measurements of a Dual-Energy Fast Photon Counting CdTe Detector with Integrated Charge Sharing Correction," *Proceedings of SPIE Medical Imaging*, vol. 8668, pp. 86680P–86680P–8, 2013.

[9] J. Jakubek, "Data processing and image reconstruction methods for pixel detectors," in *Proceedings of the 8th International Workshop on Radiation Imaging Detectors*, vol. 576, pp. 223–234, 2007.

[10] D. Vavrik, J. Dammer, T. Holy, J. Jakubek, S. Pospisil, and Z. Vykyda, "Direct thickness calibration: way to radiographic study of soft tissues," in *Proceedings of the 9th ICATPP Conference on Astroparticle, Particle, Space Physics, Detectors and Medical Physics Applications*, pp. 773–778, 2005.

[11] N. K. Strobel, B. Heigl, T. M. Brunner, O. Schütz, M. M. Mitschke, K. Wiesent, and T. Mertelmeier, "Improving 3D Image Quality of X-ray C-Arm Imaging Systems by Using Properly Designed Pose Determination Systems for Calibrating the Projection Geometry," in *Proceedings of SPIE Medical Imaging*, vol. 5030, pp. 943–954, 2003.

[12] A. Maier, H. G. Hofmann, M. Berger, P. Fischer, C. Schwemmer, H. Wu, K. Müller, J. Hornegger, J.-H. Choi, C. Riess, A. Keil, and R. Fahrig, "CONRAD – a software framework for cone-beam imaging in radiology.," *Medical Physics*, vol. 40, no. 11, p. 111914, 2013.

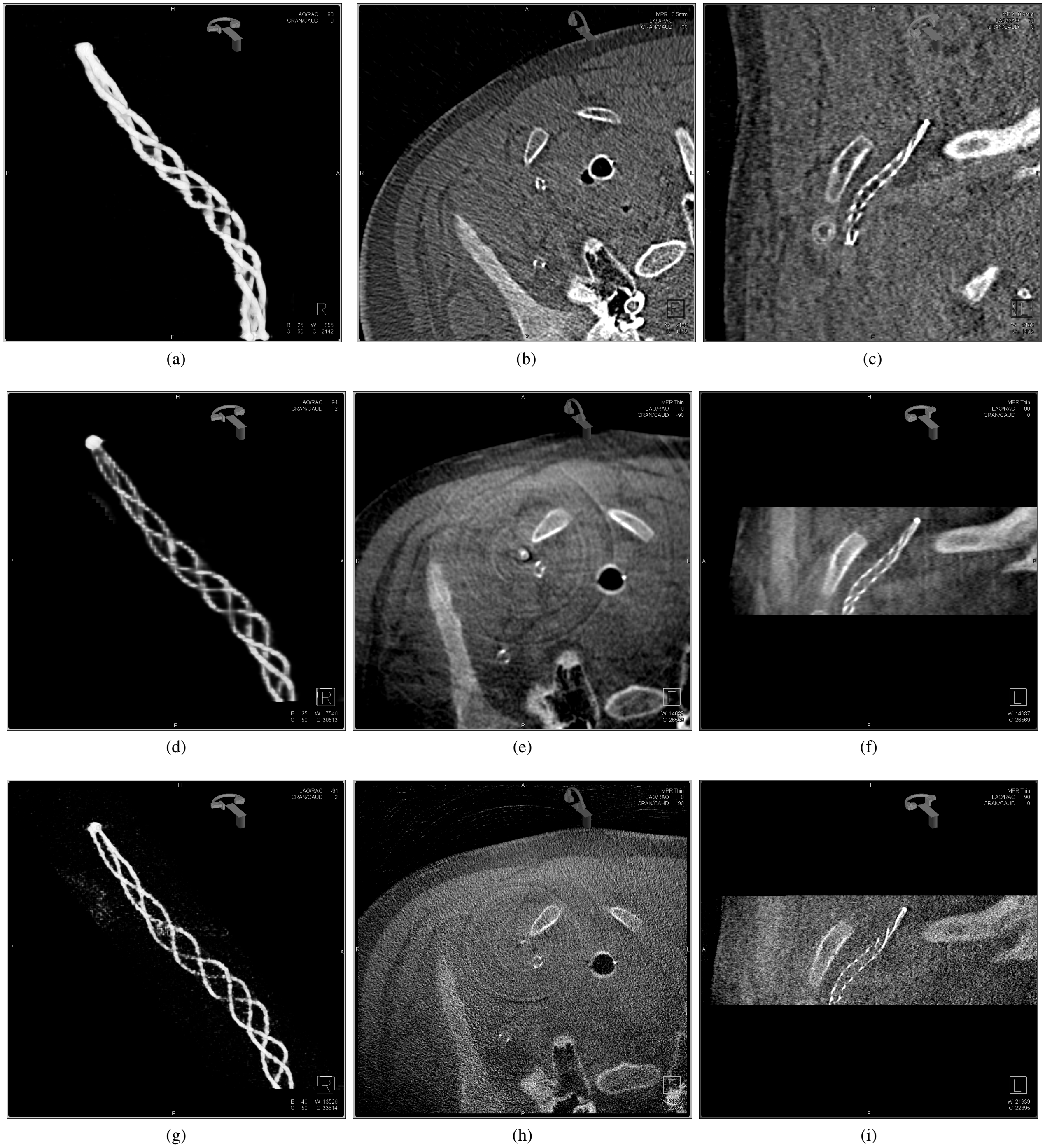


Figure 5: 3D reconstructions of the *in-vivo* pig dataset. From left to right, volume rendered image, axial slice, and sagittal view. The first row shows the FD, the second row the 3×3 binned FD-mimicked, and the third row the 1×1 XCD reconstruction.